Northumbria Research Link

UniversityLibrary

1   **Reconstructing paleoseismic deformation, 2: 1000 years of great earthquakes at Chucalén,**

2   **south central Chile**

3

4   E. Garrett [a],*, I. Shennan[a], S.A. Woodroffe[a], M. Cisternas[b], E. P. Hocking[c], and P. Gulliver[d]

5

6   [a] Durham University, Sea Level Research Unit, Department of Geography, South Road,

7   Durham, DH1 3LE, UK

8   [b] Escuela de Ciencias del Mar, Pontificia Universidad Católica de Valparaíso, Altamirano

9   1480, Valparaíso, Chile

10   [c] Northumbria University, Department of Geography, Ellison Place, Newcastle upon Tyne,

11   NE1 8ST, UK

12   [d] NERC Radiocarbon Facility, SUERC, Rankine Avenue, Scottish Enterprise Technology Park,

13   East Kilbride, G75 0QF, UK

14   *Corresponding author. Now at The Geological Survey of Belgium, Royal Belgian Institute for

15   Natural Sciences, Jennerstraat 13, 1000 Brussels, Belgium. Email:

16   egarrett@naturalsciences.be

17

18   **Abstract**

19

20   In this paper we adopt a quantitative biostratigraphic approach to establish a 1000-year-long

21   coastal record of megathrust earthquake and tsunami occurrence in south central Chile. Our

22   investigations focus on a site in the centre of the rupture segment of the largest

23   instrumentally recorded earthquake, the AD 1960 magnitude 9.5 Chile earthquake. At

24   Chucalén coseismic subsidence in 1960 is recorded in the lithostratigraphy and

25   biostratigraphy of coastal marshes, with peat overlain by minerogenic sediment and changes

26   in the assemblages of diatoms (unicellular algae) indicating an abrupt increase in relative sea

27   level. In addition to the 1960 earthquake, the stratigraphy at Chucalén records three earlier

28   earthquakes, the historically documented earthquake of 1575 and two prehistoric

29   earthquakes, radiocarbon dated to AD 1270 – 1450 and 1070 – 1220. Laterally extensive

30   sand sheets containing marine or brackish diatom assemblages suggest tsunami deposition

31   associated with at least two of the three pre-1960 earthquakes. The record presented here

32   suggests a longer earthquake recurrence interval, averaging 270 years, than the historical

33   recurrence interval, which averages 128 years. The lack of geologic evidence at Chucalén of

34   two historically documented earthquakes, in 1737 and 1837, supports the previously

35   suggested hypothesis of variability in historical earthquake characteristics. Our estimates of

36   coseismic land-level change for the four earthquakes range from meter-scale subsidence to

37   no subsidence or slight uplift, suggesting earthquakes completing each ~270 year cycle may

38   not share a common, characteristic slip distribution. The presence of buried soils at

39   elevations below their modern equivalents implies net relative sea-level rise over the course

40   of the Chucalén paleoseismic record, in contrast to relative sea-level fall over preceding

41   millennia inferred from sites on the mainland. Sea-level rise may contribute to the

42   preservation of evidence for multiple earthquakes during the last millennium, while net

43   relative sea-level fall over the last 2000 to 5000 years may explain the lack of evidence for

44   older earthquakes.

45

46   **Keywords:** Paleoseismicity, earthquake reconstruction, tsunami, relative sea level, diatoms,

47   transfer functions

48

49   **1.   Introduction**

50

51   Geological approaches to understanding the chronology and characteristics of past

52   earthquakes are essential for assessing potential future hazards posed by subduction zones

53   (Stein and Okal, 2011). Reliance on short historical records may prevent adequate

54   appreciation of the complexities of subduction zone behaviour, including the occurrence of

55   segmentation, variability in rupture magnitudes and the existence of supercycles (Cisternas

56   *et al.*, 2005; Jankaew *et al.*, 2008; Sieh *et al.*, 2008; Goldfinger *et al.*, 2012; Sawai *et al.*,

57   2012). In this paper, we adopt a quantitative lithostratigraphic and biostratigraphic approach

58   to reconstruct past earthquakes in south central Chile. The approach, developed in other

59   subduction zone settings (Atwater, 1987; Nelson *et al.*, 1996; Hamilton and Shennan, 2005),

60   is tested along the Chilean coastline in the counterpart to this paper (Garrett *et al.*, 2013).

61   Focusing on a new site at Chucalén, northern Isla de Chiloé (Fig. 1), we aim to: 1) establish

62   whether coastal sediments record evidence for multiple earthquakes and tsunamis; 2)

63   determine the timing of these ruptures; 3) contrast stratigraphic and historical records of

64   earthquakes to assess variability in historical ruptures; 4) calculate the recurrence interval

65   between earthquakes; 5) quantify vertical coseismic deformation for each earthquake and 6)

66   establish whether the record of long-term sea-level change explains the preservation or

67   absence of stratigraphic evidence for earthquakes.

68

69   The potential for great earthquakes in south central Chile is well known. The 22nd May 1960

70   Valdivia, Chile earthquake remains the largest since the inception of modern seismic

71   recording. The earthquake ruptured 1000 km of the Chilean subduction zone between the

72   Arauco Peninsula in the north and the Taitao Peninsula in the south (Fig. 1). Slip on the fault

73   locally reached 40 m, contributing to a moment magnitude (M_w) of 9.5 (Cifuentes, 1989;

74   Barrientos and Ward, 1990). The surface expression of coseismic deformation in 1960 (Fig.

75   1) featured subsidence up to 2.4 m, coinciding with the coastline, flanked by two regions of

76   uplift (Wright and Mella, 1963; Plafker and Savage, 1970). Uplift of a 100 km wide region

77   offshore locally exceeded 5 m (Plafker and Savage, 1970) and submarine deformation

78   generated a devastating local tsunami, which crested over 20 m high, and a trans-Pacific

79 tsunami more than 4 m high in Hawaii and Japan (Cox and Mink, 1963; Keys, 1963; Atwater

80 *et al.*, 2005). Along the coast of south central Chile, tidal marsh stratigraphy preserves

81 evidence for the 1960 tsunami in the form of widespread landward-thinning sand sheets

82 abruptly emplaced over intertidal marshes and adjacent organic wetland soils (Wright and

83 Mella, 1963; Cisternas *et al.*, 2000; Bourgeois, 2009; Garrett *et al.*, 2013). Records kept by

84 Spanish settlers and visiting Europeans describe three earlier large earthquakes in south

85 central Chile in 1837, 1737 and 1575 (Lomnitz, 1970); however, the recurrence of

86 earthquakes with 40 m of slip on the fault at approximately 130-year intervals would far

87 exceed the plate convergence rate, implying variability in rupture size, coseismic slip and

88 earthquake magnitude (Stein *et al.*, 1986; Barrientos and Ward, 1990). Stratigraphic

89 evidence for repeated tsunamis accompanied by subsidence in the centre of the 1960

90 segment supports a longer recurrence interval between 1960-sized earthquakes –

91 approaching 300 years – with partial strain release during smaller intervening ruptures

92 (Cisternas *et al.*, 2005). The 1737 and 1837 earthquakes are inferred to be of shorter rupture

93 length, with reduced slip, however their magnitudes and locations remain unknown

94 (Cisternas *et al.*, 2005; Vita-Finzi, 2011; Moernaut *et al.*, 2014).

95

96 **2. Study area**

97

98 The coast of Chile lies above a convergent margin, where the Nazca plate subducts beneath

99 South America at a rate averaging $60 - 80$ mm yr^{-1} (DeMets *et al.*, 1990; Angermann *et al.*,

100 1999). Strain accumulation results in the occurrence of megathrust earthquakes, great

101 ($M_w > 8$) interplate ruptures that may generate devastating tsunamis. Historical records

102 suggest along-strike segmentation of the subduction zone, with all or part of the 1960

103 rupture segment also failing in 1837, 1737 and 1575 (Lomnitz, 1970; Barrientos, 2007).

104 Geological evidence for older earthquakes is scarce; Bartsch-Winkler and Schmoll (1993) and

105   Nelson *et al*. (2009) attribute the fragmentary nature of south central Chilean coastal

106   stratigraphic records to erosion associated with falling late Holocene relative sea level.

107

108   In this study, we focus on a new site in the centre of the 1960 segment (Fig. 1). The coastal

109   lowlands and tidal marshes fringing Bahía Quetalmahue, northern Isla de Chiloé, are ideal

110   locations for the preservation of evidence for past relative sea-level change, earthquakes

111   and tsunamis due to the shelter afforded by the Lacui Peninsula to the west and north, the

112   lack of any significant fluvial input and the moderate tidal range (mean higher high water =

113   1.02m above mean sea level). The site at Chucalén, on the western margin of Bahía

114   Quetalmahue, lies approximately 25 kilometres west of the axis of maximum coseismic

115   subsidence in 1960. Based on the pre- and post-earthquake lower growth limits of terrestrial

116   vegetation, Plafker and Savage (1970) estimate Chucalén subsided coseismically by

117   1.0 ± 0.2 m in 1960.

118

119   **3. Materials and methods**

120

121   3.1 Stratigraphy

122

123   The sediment stratigraphy of tidal marshes may record evidence for vertical deformation

124   both during megathrust earthquakes and through the intervening interseismic periods

125   (Atwater, 1987; Nelson *et al*., 1996). Depending on their position with respect to the locked

126   plate interface, coasts above subduction zones may rise slowly in response to strain

127   accumulation (Fig. 2). Land uplift, experienced at the coast as a gradual fall in relative sea

128   level, is reflected in tidal marsh stratigraphy by a progressive transition from minerogenic to

129   organic sediment deposition. Depending on the location of fault slip with respect to the

130   coastline, subsequent coseismic strain release may cause near-instantaneous land

131   subsidence (Fig. 2). Experienced at the coast as a rapid rise in relative sea level, subsidence

132   leads to the abrupt emplacement of minerogenic sediments on top of organic marsh soils.

133   The distribution and magnitude of coseismic surface displacement may differ between

134   cycles in response to variation in the location of slip on the fault interface and the amount

135   and heterogeneity of the slip (Wang, 2007).

136

137   Sequences of organic intertidal soils interbedded with minerogenic units may reflect cycles

138   of seismic land-level changes (e.g. Atwater, 1987; Darienzo and Peterson, 1990; Shennan *et*

139   *al.*, 1996; Sawai *et al.*, 2002; Hamilton and Shennan, 2005); however, a range of other

140   sedimentologic, hydrographic, oceanographic and atmospheric processes can give rise to

141   similar stratigraphies (Long and Shennan, 1994; Witter *et al.*, 2001). Following Nelson *et al.*

142   (1996), we attribute organic-minerogenic couplets to coseismic subsidence only where (1)

143   couplets are laterally extensive; (2) organic sediments are buried by sediments indicative of

144   a lower elevation; (3) submergence is sudden and (4) submergence is synchronous at widely

145   spaced sites. The coincidence of submergence with tsunami deposits may also support a

146   coseismic origin (Atwater, 1987; Nelson *et al.*, 1996; Cochran *et al.*, 2005; Sawai *et al.*, 2009),

147   however tsunami deposits are fragmentary and their absence does not negate the

148   association of a sedimentary couplet with an earthquake (Nelson *et al.*, 1996).

149

150   Marsh front exposures and a perpendicular transect of 28 closely spaced hand-driven gouge

151   cores reveal the stratigraphy at Chucalén. Box samples taken from an exposure at the

152   seaward end of the coring transect provide sediment samples for laboratory and microfossil

153   analyses and dating.

154

155   3.2 Biostratigraphy

156

157   Microfossils, particularly diatoms, assist in the identification of tsunami deposits (e.g.

158   Dawson *et al.*, 1996; Hemphill-Haley, 1996) and determination of the amount and

159   suddenness of marsh elevation change (e.g. Shennan *et al.*, 1996; 1999; Sawai *et al.*, 2004).

160   Their utility for quantifying changes in land level stems from the fact that different species

161   occupy different elevations in intertidal environments. While elevation does not directly

162   influence diatom distributions, in coastal marshes it affects flooding frequency and duration,

163   salinity, organic content and grain size; key controls on diatom distributions (Vos and de

164   Wolf, 1993; Gehrels *et al.*, 2001; Patterson *et al.*, 2005)*.* Changes in fossil diatom

165   assemblages, therefore, reflect changes in the elevation of the marsh surface with respect to

166   sea level over time.

167

168   We prepare samples for diatom analysis following standard procedures (Palmer and Abbott,

169   1986), with a minimum of 250 diatom valves counted per sample. We plot assemblage

170   diagrams using C2 software package v.1.7.2 (Juggins, 2011) and provide a visual summary by

171   dividing species into two categories based on their elevation optima in the modern dataset,

172   with dark blue indicating species with optima below mean higher high water (MHHW) and

173   light blue indicating species with optima above MHHW.

174

175   We apply transfer function models to estimate the paleomarsh surface elevation associated

176   with each fossil diatom assemblage. These models incorporate contemporary intertidal

177   diatom assemblage data from four marshes in south central Chile, as detailed by Garrett *et*

178   *al.* (2013). Model selection maximizes the correlation between observed and predicted

179   elevations and minimizes the reconstruction error. The selected transfer function model has

180   a cross-validated r^2 of 0.77 and a root mean square error of prediction of 0.38 m.

181   Assessment of paleomarsh surface elevation reconstructions follow Garrett *et al.* (2013),

182   employing minimum dissimilarity coefficients (MinDC) from the Modern Analogue

183   Technique in the C2 software package (Juggins, 2011) to measure the similarity between the

184   diatom assemblages in each fossil sample and samples in the modern training set.

185

186   The conversion of paleomarsh surface elevation to estimates of relative sea level requires

187   the field elevation of each sample. We define relative sea level relative to present mean sea

188   level as:

189

190    $RSL_n = FE_n - PMSE_n$ (1)

191

192   Where:

193   RSL_n = Relative sea level estimate for sample n

194   FE_n = Field elevation of sample n (metres, present mean sea level)

195    $PMSE_n$ = Paleomarsh surface elevation (metres, mean sea level at time of deposition)

196

197   Sample specific 95% error terms are the root of the sum of the squared errors in

198   reconstructing the paleomarsh surface elevation and estimating the field elevation of

199   samples. The difference between pre- and post-earthquake RSL estimates defines the

200   magnitude of coseismic deformation.

201

202   3.3 Chronology

203

204   We base the Chucalén chronology on AMS radiocarbon dating of herbaceous plant

205   macrofossils. Where possible, we select horizontally bedded above ground parts of

206   terrestrial plants, however below ground material may contribute to samples where more

207   favourable material was lacking. We report dates as ^{14}C years BP and calibrate to 2σ age

208 ranges in years AD using the SHCal13 calibration curve (Hogg *et al.*, 2013). For samples

209 exceeding 100 % modern carbon, we employ the post-bomb atmospheric southern

210 hemisphere ^{14}C curve (Hua and Barbetti, 2004). Stratigraphic ordering allows these samples

211 to be fitted to either the rising or the falling limb of the post-bomb curve and single

212 calibration solutions to be obtained (supplementary Fig. S1). The age model uses the

213 Bayesian *P_sequence* approach in OxCal 4.2 (Bronk Ramsey, 2009).

214

215 **4.   Results**

216

217 **4.1 Stratigraphy**

218

219 Marsh front exposures at Chucalén display four abrupt transitions from organic to

220 minerogenic deposition (Fig. 3). We refer to the four buried organic units as Soils A, B, C and

221 D, with A the uppermost and D the lowermost. The buried soils are continuous and largely

222 uninterrupted for more than 300 m in marsh front exposures and a series of 28 hand-drilled

223 cores maps the couplets as they rise across tidal marsh and freshwater meadow (Fig. 3;

224 supplementary figure S2).

225

226 Buried soil A is mid to dark brown, sandy and locally contains the remains of woody plants,

227 tree stumps and other herbaceous plant material, including the rhizomes of *Spartina*

228 *densiflora* and *Juncus balticus*. The overlying one- to ten-centimetre-thick mid grey sand

229 sheet flattens and encases vegetation rooted in Soil A. The sand deposit decreases in

230 thickness with increasing distance from the marsh front and extends more than 75 m inland

231 (Fig. 2). Additional sand lenses more than 100 m inland may be a continuation of this sand

232 sheet, however their discontinuous nature precludes their unequivocal correlation.

233

234   Soil B, occurring in marsh front exposures and 17 cores at the seaward end of the coring

235   transect, is mid to dark brown and sandy (Fig. 3). It lacks the rhizomes and woody plant

236   remains found in Soil A, but contains fragments of herbaceous plants and humified organic

237   matter. A light brown to mid grey sand sheet overlies the soil and extends at least 80 m

238   inland from the marsh front. The deposit is generally thicker than the sand sheet overlying

239   Soil A, with a maximum thickness of 18 cm.

240

241   Buried soil C is mid to very dark brown and silty, with herbaceous plant remains, but no

242   woody plant material. The overlying light grey-brown silty sand sheet is generally 5 to 10 cm

243   thick, however the precise thickness of the deposit is difficult to ascertain as it grades into

244   the base of Soil B. The contact between Soil C and the minerogenic unit can be traced 80 m

245   inland from the marsh front. The upper part of the buried soil features numerous sub-

246   centimetre burrows filled with the overlying silty sand (Fig. 3; supplementary Fig. S2).

247

248   Soil D, the lowermost buried soil, is mid to very dark brown and silty, with occasional

249   herbaceous plant fragments and no woody plant remains. A light brown to mid grey silty

250   sand sheet overlies the soil. At 3 to 5 cm thick, this deposit is generally thinner than the

251   minerogenic units overlying the three other buried soils and does not extend as far inland

252   (Fig. 3).

253

254   **4.2 Chronology**

255

256   Twelve AMS radiocarbon samples provide a chronology for the Chucalén sedimentary

257   sequence (Table 1). We exclude four other dates where visual assessment and outlier

258   analysis suggest downward root penetration has resulted in younger ages than their

259   stratigraphic position would suggest. We adjust the depths to exclude three sand layers,

260   which we interpret as tsunamis (discussed in section 5.1). Bayesian age modelling in OxCal

261   v.4.2 (Bronk Ramsey, 2009) provides an age-depth model (Fig. 4) with an overall agreement

262   index of 69.1, indicating satisfactory agreement between prior and posterior age

263   distributions (Table 1). Calibrated ages indicate the sediments accumulated over the last

264   millennium. The age model constrains the timing of the abrupt upper contact of Soil A to AD

265   1955 – 1971 (Fig. 4). This supports the mid- to late-20th century age inferred from elevated

266   caesium-137 concentrations (Garrett *et al.*, 2013), and confirms the association of the burial

267   of Soil A with subsidence during the 1960 earthquake. The large range in ages for the burial

268   of Soil B, AD 1540 – 1800, reflects uncertainties introduced by calibrating dates from the

269   sixteenth to nineteenth century radiocarbon plateau. The upper contact of Soils C and D

270   date to AD 1270 – 1450 and AD 1070 – 1220 respectively (Fig. 4).

271

272   **4.3 Biostratigraphy**

273

274   Diatom assemblages in samples from the marsh front exposure contain species indicative of

275   intertidal environments (Fig. 5). Of the 143 taxa encountered, 117 occur in the modern

276   training set and 21 exceed 10 % of the total diatom count in one or more sample. Calibration

277   of assemblages using the south central Chile transfer function (Garrett *et al.*, 2013) yields

278   reconstructions of paleomarsh surface elevation, which we convert to relative sea-level

279   reconstructions (Fig. 5).

280

281   High marsh species dominate diatom assemblages from Soil A. An abrupt change to

282   assemblages containing species with a range of elevation preferences marks the transition

283   to the overlying sand sheet. After an initial peak in one species with a modelled elevation

284   optimum above mean higher high water (MHHW), the base of the modern marsh soil

285   predominantly features species with optimum elevations below MHHW.

286

287 Species typically found below MHHW occur in Soil B, with only occasional taxa from

288 environments higher in the intertidal zone. The overlying sand sheet contains increased

289 percentages of these low elevation species, with abrupt changes only observed in the

290 abundances of minor species. Immediately above the sand sheet, diatoms from the base of

291 Soil A feature increased percentages of species with optimum elevations above MHHW.

292

293 Buried Soil C contains a range of species from high marsh environments, alongside the

294 ubiquitous *Pseudostaurosira perminuta*. An abrupt decrease in the abundances of high

295 marsh species marks the boundary with the overlying silty sand. Species with optimum

296 elevations below MHHW characterise the silty sand and continue to be found in the base of

297 Soil B alongside occasional taxa from higher marsh elevations.

298

299 As found in Soil C, Soil D features high marsh species together with *Pseudostaurosira*

300 *perminuta*. While *P. perminuta* remains abundant in the overlying silty sand, the high marsh

301 species abruptly give way to low elevation taxa. Species characteristic of low intertidal

302 elevations continue to dominate assemblages from the base of Soil C.

303

304 **5.   Discussion**

305

306 **5.1 Evidence for multiple earthquakes**

307

308 The stratigraphic, microfossil and radiocarbon results from Chucalén provide evidence for

309 laterally continuous buried soils, submerged by abrupt relative sea-level rise at similar times

310 to episodes of coseismic subsidence and tsunami deposition reported by Cisternas *et al*.

311 (2005) from Maullín. We test the hypothesis that each buried soil at Chucalén records the

312   occurrence of an earthquake, focusing on the criteria outlined by Nelson *et al.* (1996),

313   evidence for tsunami deposition and the modelled timing of the burial of each soil.

314

315   *Soil A*

316   Buried soil A is laterally extensive and diatom assemblages indicate a sudden transition to

317   sediments deposited at a lower elevation. The transfer function model estimates subsidence

318   of 0.81 ± 1.04 m, increasing to 1.12 ± 1.03 m if the lowest post-earthquake sea-level

319   reconstruction, 4 cm above the upper boundary of the sand sheet, is selected (Fig. 5; Table

320   2). The magnitude of modelled subsidence is in good agreement with the 1.0 ± 0.2 m

321   documented by Plafker and Savage (1970) for the AD 1960 earthquake.

322

323   Based on local testimony, Garrett *et al.* (2013) interpret the sand sheet overlying Soil A as

324   the deposit left by the 1960 tsunami. While storms, river floods and aeolian processes may

325   also deposit sand sheets in intertidal settings, the sheltered location of the site and the lack

326   of nearby rivers or subaerial sand sources support the tsunami interpretation. We do not

327   attempt to infer the maximum landward extent of the deposit or the tsunami inundation

328   limit as ploughing and trampling by livestock precludes identification of the deposit at higher

329   elevations.

330

331   Radiocarbon age modelling constrains the timing of the abrupt burial of Soil A to AD 1955 –

332   1971 (Fig. 4), corroborating the correlation with the 1960 earthquake previously inferred

333   from ^{137}Cs concentrations (Garrett *et al.*, 2013).

334

335   *Soil B*

336   The lateral extent and abrupt nature of the upper contact support coseismic subsidence as

337   the mechanism for the burial of Soil B. The diatom data, however, do not suggest that the

338   soil is overlain by sediments indicative of a lower elevation. On the contrary, there is a net

339   sea-level fall between the top of Soil B and the bulk of Soil A (Table 2), clearly reflected in

340   the diatom assemblages, although the 95% error terms for the reconstructions and number

341   of poor modern analogues (Fig. 5) point to the need for a larger modern dataset to improve

342   the transfer function models. The diatom assemblages in the basal 1 cm of Soil A are more

343   transitional, but they could either reflect a mix of the assemblages from the sand with those

344   of the new environment developing on an uplifted marsh, or suggest there is no elevation

345   change across the sand, followed by gradual relative sea-level fall.

346

347   We interpret the sand layer overlying Soil B as a tsunami deposit. Like the 1960 tsunami

348   deposit, this sand layer is laterally extensive and coarse grained, with well-defined lower and

349   upper contacts. Diatom assemblages indicate a marine rather than fluvial or terrestrial

350   sediment source. The highly enclosed nature of Bahía Quetalmahue does not favour storm

351   surges as a mechanism for the emplacement of decimetre-thick sand sheets at Chucalén.

352

353   The timing of burial, AD 1540 – 1800, overlaps with two major historical earthquakes in 1575

354   and 1737. While other processes cannot yet be completely discounted, we suggest the 1575

355   earthquake and tsunami provides the most plausible candidate for the stratigraphy at

356   Chucalén. At Maullín, 45 km to the northeast, Cisternas *et al.* (2005) present sedimentary,

357   dendrochronological and documentary evidence for coseismic subsidence and tsunami

358   inundation in 1575. While the 1737 earthquake also falls within the age range of the burial

359   of Soil B at Chucalén, historical records do not mention a tsunami associated with this

360   earthquake (Lomnitz, 1970; Cisternas *et al*., 2005) and there is no geological evidence for the

361   earthquake or tsunami at Maullín (Cisternas *et al.*, 2005).

362

363   We conclude that the simplest explanation for the burial of Soil B and net uplift between the

364   top of Soil B and the bulk of Soil A is either coseismic uplift or no coseismic elevation change

365   followed by rapid post-seismic uplift. The latter would imply a spatial pattern of coseismic

366   and post-seismic motions similar to that described by Sawai *et al.* (2004) from Japan; and

367   both explanations imply a different pattern of rupture and surface deformation for the 1960

368   and 1575 earthquakes. We highlight that this reconstruction comes from a single exposure

369   and that local factors such as erosion of the surface of Soil B could impact on the magnitude

370   of deformation recorded.

371

372   *Soil C*

373   Found throughout the lower half of the coring transect, Soil C is laterally extensive and

374   abruptly overlain by sediments containing diatom assemblages indicative of a lower

375   intertidal elevation (Fig. 5). The estimated magnitude of deformation depends on the

376   interpretation of the minerogenic unit overlying the buried soil. The upper contact of the soil

377   is clearly defined, but in the sampled exposure the presence of burrows filled with the

378   overlying silty sand suggests bioturbation. Cisternas *et al*. (2005) note the similar appearance

379   of a buried soil at Maullín and propose that this reflects post-subsidence erosion and

380   burrowing by intertidal organisms. Abruptly emplaced tsunami sand sheets may mantle

381   soils, preventing bioturbation and maintaining the intact nature of the contact. If no tsunami

382   sediment was deposited on Soil C at this particular location, the minerogenic sediments

383   overlying the soil accumulated after the earthquake and are therefore indicative of the post-

384   earthquake land level. Comparison of diatom assemblages across the contact suggests

385   subsidence of 0.92 ± 1.20 m (Table 2). If the minerogenic unit incorporates reworked

386   tsunami-lain sediment, the diatom assemblages may not reflect the post-earthquake land

387   level. Comparison of samples from Soil C and the base of Soil B suggests subsidence of

388   0.69 ± 1.17 m.

389

390   The age model constrains the timing of the burial of Soil C to AD 1270 – 1450 (Fig. 4). This

391   overlaps the most recent prehistoric earthquake recorded at Maullín, AD 1280 – 1390

392   (Cisternas *et al.*, 2005), supporting the occurrence of synchronous submergence at different

393   sites.

394

395   *Soil D*

396   The lowermost buried soil is laterally extensive, found in 14 of the 28 cores and in marsh

397   front exposures, and abruptly overlain by a tabular silty sand deposit. Comparison of diatom

398   assemblages from the top of Soil D and the base of Soil C using the transfer function model

399   suggests abrupt subsidence of 0.60 ± 1.10 m (Fig. 5; Table 2). While the lack of good modern

400   analogues for the assemblages encountered in Soil D again highlights the need for a larger

401   modern dataset, the reconstructed relative sea levels make ecological sense given the

402   distribution of the major species in the modern environment.

403

404   As with the minerogenic layers overlying Soils A and B, tsunami deposition is the favoured

405   hypothesis for the emplacement of the silty sand sheet overlying Soil D. The abundant low

406   elevation diatoms found in this unit indicate a marine sediment source (Fig. 5). The lack of

407   evidence for bioturbation of Soil D and a relatively well defined upper contact at the base of

408   Soil C favour tsunami deposition over gradual sediment accumulation on a post-subsidence

409   tidal flat.

410

411   The timing of the burial of Soil D, AD 1070 – 1220, closely corresponds to the age range of

412   evidence for subsidence and tsunami inundation at Maullín, AD 1020–1180 (Cisternas *et al.*,

413   2005).

414

415   **5.2 Variability in historical earthquake ruptures**

416

417   When compared to historical records of earthquakes, coastal sediments at Chucalén appear

418   to underrepresent the frequency of major earthquakes in south central Chile. The absence

419   of evidence for the 1737 and 1837 earthquakes at Chucalén suggests variability in the

420   characteristics of the historical ruptures. Several lines of evidence suggest the 1737 and

421   1837 earthquakes ruptured smaller areas of the plate interface and generated less damaging

422   tsunamis than the earthquakes of 1575 and 1960 (Lomnitz, 1970; Cisternas *et al.*, 2005;

423   Moernaut *et al.*, 2014). The 1737 earthquake produced isolated accounts of damage in

424   Valdivia and Chiloé (Lomnitz, 1970, Cisternas *et al.*, 2005). The lack of any reports of tsunami

425   occurrence may reflect the location of the rupture with respect to populated areas or the

426   faulting mechanism not resulting in a large tsunami. Using a quantitative lacustrine turbidite

427   approach, Moernaut *et al.* (2014) suggest the 1737 earthquake ruptured an area to the

428   north of Chiloé. Like at Maullín (Cisternas *et al.*, 2005), we find no evidence for the 1737

429   earthquake at Chucalén. The lack of deformation implies a different rupture pattern to that

430   associated with the 1960 earthquake and is consistent with the rupture area proposed by

431   Moernaut *et al*. (2014).

432

433   While the 1837 earthquake produced a large trans-Pacific tsunami, records of the tsunami

434   are not as widespread along the Chilean coast as in 1575 and 1960, with no reports of

435   extensive damage (Lomnitz, 1970; Lander and Lockridge, 1989; Atwater *et al*., 2005).

436   Coseismic uplift in the Chonos Archipelago may suggest a rupture area in the southern half

437   of the 1960 segment (Lomnitz, 1970). While Concepción experienced intense shaking

438   (Cisternas *et al.*, 2005) and the earthquake triggered turbidites in lakes north east of Valdivia

439   (Moernaut *et al.*, 2014) and in Reloncaví Fjord (St-Onge *et al.*, 2012), neither the stratigraphy

440   nor the biostratigraphy at Chucalén shows evidence for tsunami inundation or abrupt

441   changes in relative sea level during this period (Fig. 5). Combined with the lack of evidence

442   for deformation at Maullín (Cisternas *et al.*, 2005), we suggest the northern extent of the

443   1837 rupture lies to the south of northern Chiloé or that any slip occurring in this region was

444   minimal. This interpretation is consistent with a rupture length of up to 500 km and does not

445   preclude near-trench strain release as proposed by Moernaut *et al*. (2014).

446

447   **5.3 Recurrence of great Chilean earthquakes**

448

449   The paleoseismic record at Chucalén spans a period approximately twice as long as that

450   covered by historical records. While the four historically documented earthquakes in 1960,

451   1837, 1737 and 1575 have an average recurrence interval of 128 years, the Chucalén record

452   suggests a longer interval, averaging approximately 270 years. Our modelled earthquake

453   ages are consistent with dates for subsidence and tsunami deposition at Maullín (Cisternas

454   *et al.*, 2005; Fig. 6). Furthermore, the timing of earthquakes in the Chucalén record coincides

455   with evidence for intense shaking from turbidites in lakes Villarica, Calafquén and Riñihue,

456   located approximately 300 km to the north (Fig. 6). In these lakes, a varve-counting

457   procedure further constrains the timing of two proposed full-segment ruptures to AD 1319 ±

458   9 years and AD 1127 ± 44 years (Moernaut *et al*., 2014).

459

460   **5.4   Implications for earthquake deformation cycles**

461

462   Evidence from Chucalén, Maullín and lakes north east of Valdivia suggests partial ruptures

463   featuring less coseismic slip in 1737 and 1837 occurred in the interval between full segment

464   ruptures in 1575 and 1960. Moernaut *et al*. (2014) identify evidence for an additional,

465   previously unrecognised earthquake, dated to AD 1466 ± 4 years. The low seismic intensity

466   inferred from their lacustrine turbidite records and the lack of evidence for deformation or

467   tsunami inundation at coastal sites in the centre of the 1960 rupture area (Cisternas *et al.*,

468   2005; this study) suggest this earthquake constitutes another partial segment rupture.

469   Cisternas *et al.* (2005) assert that stress held over smaller ruptures contributed to the size of

470   the 1960 earthquake; the identification of an earlier partial rupture suggests this process

471   could also have contributed to the size of pre-1960 full segment earthquakes.

472

473   In addition to supporting the occurrence of a bimodal rupture pattern featuring both partial

474   and full segment ruptures, the paleoseismic record from Chucalén also suggests possible

475   variability in the characteristics of the proposed full segment ruptures, reflected by

476   estimates of coseismic deformation (Fig. 5; Table 2). The earthquakes of 1960 and AD 1270 –

477   1450 appear similar at Chucalén; that of AD 1070 – 1220 produced less subsidence, whereas

478   that of AD 1575 may have entailed no subsidence or even slight uplift. In contrast, historical

479   records of the 1575 earthquake share extensive similarities with the damage, deformation

480   and tsunami inundation observed in 1960 (Lomnitz, 1970; Cisternas *et al.*, 2005). Lacustrine

481   turbidites suggest that the 1575 and 1960 earthquakes featured similar seismic intensities in

482   the northern half of the segment (Moernaut *et al.*, 2014), with marine turbidites from the

483   centre of the 1960 rupture zone also displaying similar thicknesses for the two earthquakes

484   (St-Onge *et al.*, 2012). We stress that our finding of differential deformation is only from a

485   single location at present and could reflect the limitations of the modern dataset or site-

486   specific processes. Further quantitative estimates are needed to confirm or refute the

487   magnitude of deformation inferred by this study. If confirmed, a lack of subsidence in 1575

488   at Chucalén could indicate a different spatial pattern of slip during this earthquake. We

489   suggest that this could reflect less slip in the vicinity of northern Chiloé, or slip further down-

490   dip, moving the boundary between zones of uplift and subsidence to the east of its position

491   in 1960 (Fig. 1). At present there are too few studies using quantitative reconstructions of

492   surface deformation based on paleoseismic evidence to differentiate between detailed

493   models of rupture dimensions. We have some constraints on the spatial patterns of

494   deformation, but insufficient detail to estimate the depth of the slip patch or the amount of

495   slip. Research on other subduction zones demonstrates the potential for coastal

496   paleoseismology to constrain rupture parameters (e.g. Sawai *et al.*, 2004, Wang *et al.*, 2013;

497   Shennan *et al.*, 2014) and shows how quantitative paleoseismology in Chile may progress.

498   We also advocate the need for continued and enhanced integration of coastal deformation

499   and tsunami records with earthquake reconstructions from lacustrine and marine turbidites

500   to determine the characteristics of both full and partial segment ruptures in south central

501   Chile.

502

503   **5.5 Long-term relative sea-level change**

504

505   Long-term sea-level rise provides accommodation space and promotes sediment

506   accumulation and the preservation of stratigraphic evidence for earthquakes in intertidal

507   environments (Dura *et al.*, 2011; Grand Pre *et al.*, 2012). In this section we assess the

508   evidence for long-term relative sea-level change at Chucalén and discuss the implications for

509   the length of the paleoseismic record at this site.

510

511   The occurrence of organic marsh soils at elevations below their contemporary elevation of

512   formation implies relative sea-level rise over the course of the Chucalén record. Figure 7

513   compares relative sea-level estimates derived from our model estimates and field elevations

514   at Chucalén with published data from the estuary of the Río Maullín on the adjacent

515   mainland (Atwater *et al.*, 1992). Discarding a single point from Maullín located below

516   present sea level due to the likelihood of compaction, as noted by the original authors, we

517   see a clear contrast between the datasets. The relative sea-level rise seen over the last 1000

518   years at Chucalén is not the dominant mid to late Holocene trend at Maullín, where tidal

519   marsh sediments above their contemporary depositional elevations suggest net relative sea-

520 level fall over the last 2000 to 5000 years (Atwater *et al.*, 1992). Glacial isostatic adjustment

521 models also suggest falling relative sea level characterized the Pacific coast of South America

522 during the late Holocene (Fig. 7; Peltier, 2004). Falling sea level reduces accommodation

523 space and favours erosion over sediment deposition. Nelson *et al.* (2009) evoke this process

524 for the scarcity of paleoseismic evidence in the Valdivia estuary; falling relative sea level may

525 also explain the lack of evidence for earthquakes older than ~ AD 1100 at Chucalén.

526

527 The causes of sea-level rise at Chucalén over the last millennium remain equivocal and could

528 relate to the magnitude of coseismic subsidence exceeding interseismic uplift, regional

529 tectonics, isostatic subsidence due to the collapse of a neoglacial forebulge or eustasy, while

530 site-specific factors including compaction could also contribute. The discrepancy between

531 observations and models of late Holocene Chilean relative sea level is not currently

532 adequately explained and deserves further investigation.

533

534 **6. Conclusions**

535

536 Laterally extensive buried soils with abrupt upper contacts and evidence for rapid and

537 substantial marsh surface elevation change suggest sediments at Chucalén record evidence

538 for repeated great earthquakes. The major conclusions of our work are:

539 1. Predecessors of the 1960 great earthquake occurred in AD 1540 – 1800, 1270 – 1450

540 and 1070 – 1220. These ages closely correspond with maximum ages for tsunami

541 deposition and submergence at Maullín (Cisternas *et al.*, 2005) and turbidite

542 deposition in lakes north east of Valdivia (Moernaut *et al.*, 2014). We interpret the

543 sequence as including evidence for two historically documented earthquakes and

544 tsunamis, in 1575 and 1960.

545 2. The lack of evidence for tsunami deposition and land-level change corresponding to

546   historically documented earthquakes in 1737 and 1837 supports the hypothesis of

547   variability in historical earthquake rupture zones. We suggest the earthquakes

548   absent from the Chucalén stratigraphy had smaller rupture zones to the north or

549   south of northern Chiloé.

550   3. The Chucalén record underrepresents the frequency of great earthquakes in south

551   central Chile. The recurrence interval between the four earthquakes, approximately

552   270 years, is more than twice the interval inferred from historical records.

553   4. Vertical coseismic deformation estimates vary between earthquakes. Diatom

554   assemblages indicate decimetre to metre-scale subsidence at Chucalén in AD 1960

555   and AD 1270 – 1450, approximately half that in AD 1070 – 1220, and no subsidence

556   or even slight uplift in AD 1575. Earthquakes completing each ~270 year cycle may

557   not share a common, characteristic slip distribution; however, there are currently

558   too few quantitative estimates of deformation to differentiate between detailed

559   models of the distribution, depth or the amount of coseismic slip.

560   5. In contrast to relative sea-level fall over the last 2000 to 5000 years inferred from

561   sites on the mainland, the presence of stacked sequences of buried soils implies

562   rising relative sea levels over the last 1000 years at Chucalén. A shift from sea-level

563   fall to sea-level rise may explain the preservation of earthquakes during the last

564   millennium and the absence of older evidence.

565   6. Quantitative paleoseismology based on coastal marshes in Chile is still at an early

566   stage compared to some other subduction zones but the results described here

567   demonstrate the potential of such methods and indicate some ways ahead for

568   future investigations through the development of more extensive modern training

569   sets to quantify land surface deformation at a larger number of coastal sites. This

570   will provide better data to constrain models of segment ruptures, including depth

571   and amount of slip.

572

583   **References**

584

585   Angermann, D., Klotz, J., Reigber, C., 1999. Space-geodetic estimation of the Nazca-South

586   America Euler vector. *Earth and Planetary Science Letters,* 171, 329-334.

587   Atwater, B. F. 1987. Evidence for Great Holocene earthquakes along the outer coast of

588   Washington State. *Science,* 236, 942-944.

589   Atwater, B., Jiménez, H., Vita-Finzi, C. 1992. Net late Holocene emergence despite

590   earthquake- induced submergence, South Central Chile. *Quaternary International*, 15/16,

591   77-85.

592   Atwater, B.F., Musumi-Rokkaku, S., Satake, K., Tsuji, Y., Ueda, K., Yamaguchi, D., 2005. *The*

593   *Orphan Tsunami of 1700.* Virginia, United States Geological Survey.

594   Barrientos, S. E. 2007. Earthquakes in Chile. *In:* MORENO, T., GIBBONS, W. (eds.) *The*

595   *Geology of Chile.* London: The Geological Society. pp. 263-287.

596   Barrientos, S.E., Ward, S.N., 1990. The 1960 Chile Earthquake – inversion for slip distribution

597   from surface deformation. *Geophysical Journal International,* 103, 589-598.

598   Bartsch-Winkler, S., Schmoll, H. 1993. Evidence for late Holocene relative sea-level fall from

599   reconnaissance stratigraphical studies in an area of earthquake-subsided intertidal

600   deposits, Isla Chiloé, southern Chile. In: Frostwick, L. E., Steel, R. J. (eds.) *Tectonic controls*

601   *and signatures in sedimentary successions.* International Association of Seismologists. pp.

602   91-108.

603   Bourgeois, J., 2009. Geologic effects and records of tsunamis. In: Robinson, A.R. and

604   Bernard, E.N., eds., The Sea, Volume 15: Tsunamis. Harvard University Press, p. 53-91.

605   Bronk Ramsey, C., 2009. Bayesian Analysis of Radiocarbon Dates. *Radiocarbon,* 51, 337-360.

606   Cifuentes, I. L., 1989. The 1960 Chilean earthquake. *Journal of Geophysical Research,* 94,

607   665-680.

608   Cisternas, M., Contreras, I., Araneda, A. 2000., Recognition and characterisation of the

609   sedimentary facies deposited by the 1960 tsunami in the Maullín estuary, Chile. *Revista*

610   *Geologica De Chile,* 27, 3-11.

611   Cisternas, M., Atwater, B. F., Torrejon, F., Sawai, Y., Machuca, G., Lagos, M., Eipert, A.,

612   Youlton, C., Salgado, I., Kamataki, T., Shishikura, M., Rajendran, C. P., Malik, J. K., Rizal, Y.,

613   Husni, M., 2005. Predecessors of the giant 1960 Chile earthquake. *Nature,* 437, 404-407.

614   Cochran, U., Berryman, K.R., Mildenhall, D.C., Hayward, B.W., Southall, K., Hollis, C.J., 2005.

615   Towards a record of Holocene tsunami and storms for Northern Hawke's Bay, New

616   Zealand. *New Zealand Journal of Geology and Geophysics,* 48, 507–515.

617   Cox, D., Mink, J. F., 1963. The Tsunami of 23 May 1960 in the Hawaiian Islands, *Bulletin of*

618   *the Seismological Society of America*, 53, 1191-1209

619   Darienzo, M.E., Peterson, C.D., 1990. Episodic tectonic subsidence of late Holocene salt

620   marshes, Northern Oregon coast, central Cascadia margin, U.S.A. *Tectonics*, 9, 1-22.

621   Dawson, S., Smith, D.E., Ruffman, A., Shi, S. 1996. The diatom biostratigraphy of tsunami

622   sediments: Examples from recent and middle Holocene events. *Physics and Chemistry of*

623   *the Earth*, 21, 87-92

624   Demets, C., Gordon, R. G., Argus, D. F., Stein, S., 1990. Current plate motions. *Geophysical*

625   *Journal International,* 101, 425-478.

626   Dura, T., Rubin, C.M., Kelsey, H.M., Horton, B.P., Hawkes, A., Vane, C.H., Daryono, M., Grand

627   Pre, C., Ladinsky, T., Bradley, S. 2011. Stratigraphic record of Holocene coseismic

628   subsidence, Padang, West Sumatra. *Journal of Geophysical Research: Solid Earth* 116,

629   B11306.

630   Garrett, E., Shennan, I., Watcham, E.P., Woodroffe, S.A., 2013. Reconstructing paleoseismic

631   deformation, 1: modern analogues from the 1960 and 2010 Chilean great earthquakes.

632   *Quaternary Science Reviews, 75, 11-21*

633 Gehrels, W. R., Roe, H. M., Charman, D. J. 2001. Foraminifera, testate amoebae and diatoms

634   as sea-level indicators in UK saltmarshes: a quantitative multiproxy approach. *Journal of*

635   *Quaternary Science,* 16, 201-220.

636 Goldfinger, C.; Nelson, C.H., Morey, A., Johnson, J.E., Gutierrez-Pastor, J., Eriksson, A.T.,

637   Karabanov, E., Patton, J., Gracia, E., Enkin, R., Dallimore, A., Dunhill, G., Vallier, T. 2012.

638   Turbidite event history: Methods and implications for Holocene Paleoseismicity of the

639   Cascadia Subduction Zone. United States Geological Survey Professional Paper 1661-F, 184

640   pp.

641 Grand Pre, C. A., Horton, B.P., Kelsey, H. M., Rubin, C.M., Hawkes, A.D., Daryono, M.R.,

642   Rosenberg, G., Culver, S.J. 2012. Stratigraphic evidence for an early Holocene earthquake

643   in Aceh, Indonesia. *Quaternary Science Reviews*, 54, 142-151.

644 Hamilton, S., Shennan, I., 2005. Late Holocene relative sea-level changes and the earthquake

645 deformation cycle around upper Cook Inlet, Alaska. *Quaternary Science Reviews,* 24, 1479-

646 1498.

647 Hemphill-Haley, E., 1996. Diatoms as an aid in identifying late-Holocene tsunami deposits.

648   *The Holocene*, 6, 439-448.

649 Hogg, A.G., Hua, Q., Blackwell, P.G., Niu, M., Buck, C.E., Guilderson, T.P., Heaton, T.J.,

650   Palmer, J.G., Reimer, P.J., Reimer, R.W., Turney, C.S.M., Zimmerman, S.R.H., 2013. SHCal13

651   Southern Hemisphere Calibration, 0-50,000 Years cal BP. *Radiocarbon,55*(4).

652 Hua, Q., Barbetti, M., 2004. Review of tropospheric bomb C-14 data for carbon cycle

653   modelling and age calibration purposes. *Radiocarbon*, 46, 1273-1298.

654 Jankaew, K., Atwater, B., Sawai, Y., Choowong, M., Charoentitirat, T., Martin, M.E.,

655   Prendergast, A., 2008. Medieval forewarning of the 2004 Indian Ocean tsunami in Thailand.

656   *Nature,* 405, 1228-1231.

657 Juggins, S. 2011. *C2 software package*. Newcastle University

658 Keys, J.G., 1963. The tsunami of 22 May 1960, in the Samoa and Cook Islands, *Bulletin of the*

659 *Seismological Society of America*, 53, 1211-1227.

660 Lander, J. F., Lockridge, P. A., 1989, *United States tsunamis 1690-1988*. National Geophysical

661 Data Center publication, v. 41-42.

662 Lomnitz, C. L., 1970. Major earthquakes and tsunamis in Chile during the period 1535 to

663 1955. *Geologische Rundshau,* 59, 938-960.

664 Long, A.J., Shennan, I., 1994. Sea level changes in Washington and Oregon and the

665 "Earthquake deformation cycle". *Journal of Coastal Research*, 10, 825-838.

666 Moernaut, J., Van Daele, M., Heirman, K., Fontijn, K., Strasser, M., Pino, M., Urruita, R., de

667 Batist, M. 2014. Lacustrine turbidites as a tool for quantitative earthquake reconstruction:

668 New evidence for a variable rupture mode in south central Chile. *Journal of Geophysical*

669 *Research,* 119, 1607-1633.

670 Nelson, A. R., Shennan, I., Long, A. J., 1996. Identifying coseismic subsidence in tidal-wetland

671 stratigraphic sequences at the Cascadia subduction zone of western North America.

672 *Journal of Geophysical Research-Solid Earth,* 101, 6115-6135.

673 Nelson, A. R., Kashima, K., Bradley, L. A. 2009. Fragmentary Evidence of Great-Earthquake

674 Subsidence during Holocene Emergence, Valdivia Estuary, South Central Chile. *Bulletin of*

675 *the Seismological Society of America,* 99, 71-86.

676 Palmer, A.J.M., Abbott, W.H. 1986. *Diatoms as indicators of sea-level change*. In van de

677 Plassche, O. (editor), *Sea-level research*. Free University, 457-87.

678 Patterson, R. T., Dalby, A. P., Roe, H. M., Guilbault, J. P., Hutchinson, I., Clague, J. J. 2005.

679 Relative utility of foraminifera, diatoms and macrophytes as high resolution indicators of

680 paleo-sea level in coastal British Columbia, Canada. *Quaternary Science Reviews,* 24, 2002-

681 2014.

682 Peltier, W.R., 2004. Global glacial isostasy and the surface of the ice-age earth: The ICE-5G

683 (VM2) model and GRACE. *Annual Review of Earth and Planetary Sciences*, 32, 111-149.

684   Plafker, G., Savage, J. C., 1970. Mechanisms of Chilean earthquakes of May 21 and May 22,

685   1960. *Geological Society of America Bulletin,* 81, 1001-1030.

686   Sawai, Y., Jankaew, K., Martin, M.E., Prendergast, A., Choowong, M., Charoentitirat, T. 2009.

687   Diatom assemblages in tsunami deposits associated with the 2004 Indian Ocean tsunami at

688   Phra Thong Island, Thailand. *Marine Micropaleontology,* 73, 70-79.

689   Sawai, Y., Namegaya, Y., Okamura, Y., Satake, K., Shishikura, M., 2012. Challenges of

690   anticipating the 2011 Tohoku earthquake and tsunami using coastal geology. *Geophysical*

691   *Research Letters* 39, L21309.

692   Sawai, Y., Nasu, H., Yasuda, Y. 2002. Fluctuations in relative sea-level during the past 3000 yr

693   in the Onnetoh estuary, Hokkaido, northern Japan. *Journal of Quaternary Science,* 17, 607-

694   622.

695   Sawai, Y., Satake, K., Kamataki, T., Nasu, H., Shishikura, M., Atwater, B., Horton, B.P., Kelsey,

696   H., Nagumo, T., Yamaguchi, M., 2004. Transient uplift after a 17th-century earthquake

697   along the Kuril subduction zone. *Science* 306, 1918–1920.

698   Shennan, I., Long, A.J., Rutherford, M.M., Green, F.M., Innes, J.B., Lloyd, J.M., Zong, Y.,

699   Walker, K.J., 1996. Tidal marsh stratigraphy, sea-level change and large earthquakes, I: A

700   5000 year record in Washington, USA. *Quaternary Science Reviews,* 15, 1023-1059.

701   Shennan, I., Scott, D. B., Rutherford, M., Zong, Y. Q. 1999. Microfossil analysis of sediments

702   representing the 1964 earthquake, exposed at Girdwood Flats, Alaska, USA. *Quaternary*

703   *International,* 60, 55-73.

704   Shennan, I., Barlow, N., Carver, G., Davies, F., Garrett, E., Hocking, E. 2014. Great

705   tsunamigenic earthquakes during the past 1000 yr on the Alaska megathrust. *Geology*, 42,

706   687-690.

707   Sieh, K., Natawidjaja, D.H., Meltzner, A.J., Shen, C.-C., Cheng, H., LI, K.-S., Suwargadi, B.W.,

708   Galetzka, J., Philibosian, B., Edwards R.L., 2008. Earthquake supercycles inferred from sea-

709   level changes recorded in the corals of west Sumatra. *Science* 322, 1674–1678.

710　St-Onge, G., Chapron, E., Mulsow, S., Salas, M., Viel, M., Debret, M., Debret, M., Foucher, A.,

711　　Mulder, T., Winiarski, T., Desmet, M., Costa, P.J.M., Ghaleb, B., Jaouen, A., Locat, J. 2012.

712　　Comparison of earthquake-triggered turbidites from the Saguenay (Eastern Canada) and

713　　Reloncavi (Chilean margin) Fjords: Implications for paleoseismicity and

714　　sedimentology. *Sedimentary Geology*, 243, 89-107.

715　Stein, S., Engeln, J. F., Demets, C., Gordon, R. G., Woods, D., Lundgren, P., Argus, D., Stein, C.,

716　　Wiens, D. A. 1986. The Nazca-South America convergence rate and the recurrence of the

717　　great 1960 Chilean earthquake. *Geophysical Research Letters,* 13, 713- 716.

718　Vita-Finzi, C. 2011. Misattributed tsunami: Chile, Sumatra and the subduction model.

719　　*Proceedings of the Geologists' Association* 122, 343-346.

720　Wang, P.-L., Engelhart, S. E., Wang, K., Hawkes, A. D., Horton, B. P., Nelson, A. R., Witter, R.

721　　C., 2013. Heterogeneous rupture in the great Cascadia earthquake of 1700 inferred from

722　　coastal subsidence estimates. *Journal of Geophysical Research: Solid Earth*,

723　　doi:10.1002/jgrb.50101.

724　Witter, R. C., Kelsey, H. M., Hemphill-Haley, E. 2001, Pacific storms, El Nino and Tsunamis,

725　　Competing mechanisms for sand deposition in a coastal marsh, Euchre Creek, Oregon,

726　　*Journal of Coastal Research*, 17, 563-583.

727　Wright, C., Mella, A., 1963. Modifications to the soil pattern of south-central Chile resulting

728　　from seismic and associated phenomena during the period May to August 1960.

729　　*Seismological Society of America Bulletin,* 53, 1367-1402.

730   **Figure captions**

731

732   Figure 1: Tectonic setting of the Chilean subduction zone and the location of the field site. a.

733   Spatial distribution of zones of uplift (blue ellipses; lighter shading where inferred) and

734   subsidence (red ellipse) during the 1960 earthquake (following Plafker and Savage, 1970); b.

735   Bahía Quetalmahue, northern Isla de Chiloé. Cisternas *et al.* (2005) studied the paleoseismic

736   site at Rio Maullín; c. the coring transect across tidal and freshwater meadow at Chucalén,

737   western Bahía Quetalmahue.

738

739   Figure 2: Schematic cross-section of a subduction zone showing vertical deformation during

740   phases of interseismic strain accumulation (top) and coseismic strain release (bottom),

741   modified from Hyndman and Wang (1993).

742

743   Figure 3: Stratigraphy of the coring transect at Chucalén, including a photograph of the

744   sampled exposure with the four buried soils labelled A – D. Divisions on photograph scale

745   bar = 10 cm. The exposure provides the sediments for diatom and radiocarbon analyses

746   reported here.

747

748   Figure 4: *P-sequence* age-depth model for the Chucalén exposure, based on radiocarbon

749   dates in Table 1. We calibrate post-bomb samples using the post-bomb atmospheric

750   southern hemisphere ^{14}C curve (Hua and Barbetti, 2004) and enter them into OxCal v.4.2

751   (Bronk Ramsey, 2009) as *C_Dates* to make use of the unique solutions inferred from

752   matching samples to the rising and falling limbs of the calibration curve (supplementary

753   Figure S1). We calibrate pre-bomb samples using the SHCal13 calibration curve (Hogg *et al.*,

754   2013). We adjust the sample depths to exclude the sand layers overlying Soils A, B and D,

755   which we interpret as tsunamis (discussed in section 5.1).

756

757   Figure 5: Summary of Chucalén diatom assemblages and relative sea-level reconstruction

758   derived from calibration of assemblages using the south central Chile transfer function

759   (Garrett *et al.*, 2013). Species classified as sub- or supra-MHHW based on modern species

760   elevation optima derived from the transfer function. We use the distance to the closest

761   modern analogue from the modern analogue technique in the C2 software package (Juggins,

762   2011) to assess the similarity between modern and fossil assemblages.
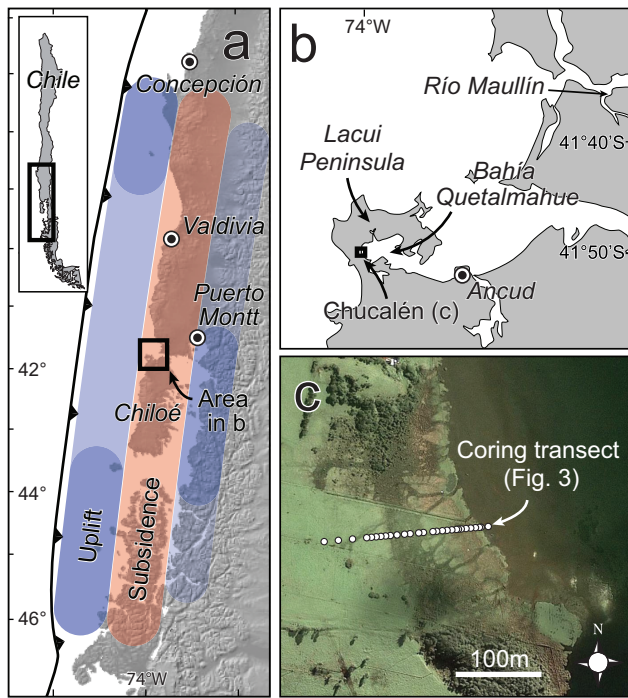
763

764   Figure 6: Comparison of the timing of earthquakes inferred from varve-dated turbidites from

765   three lakes to the north east of Valdivia (Moernaut *et al.*, 2014), pooled radiocarbon ages

766   primarily from plants killed by subsidence at Maullín (Cisternas *et al.*, 2005), *P_sequence*

767   modelling of radiocarbon dates at Chucalén (this study) and historically documented

768   earthquakes. Data from Chucalén and Maullín presented as calibrated radiocarbon date

769   probability distributions; Maullín data provide maximum ages for each earthquake; turbidite

770   ages expressed as median age from repeated varve counts (circles), with the error

771   (horizontal lines) being the difference between the median and outermost counts.

772   Additional lacustrine turbidites (ages not plotted) suggest further ruptures of smaller

773   coseismic slip and extent in AD 1466 ± 4 years, AD 1737 and AD 1837 (Moernaut *et al.*,
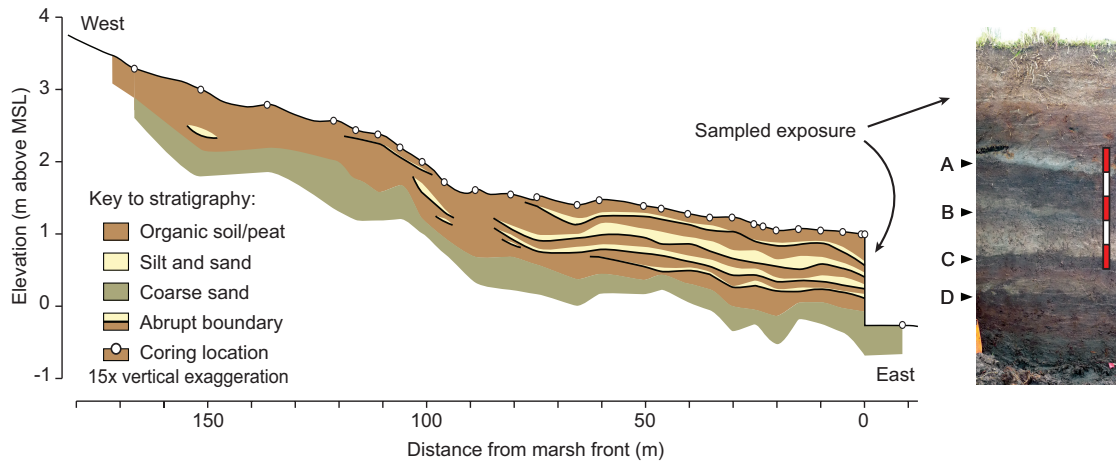
774   2014).

775

776   Figure 7: Relative sea-level change at Chucalén in a regional mid to late Holocene context.

777   This figure replicates the relative sea-level reconstructions in Figure 5, with the addition of

778   age ranges for each sample derived from the age model in Figure 4.
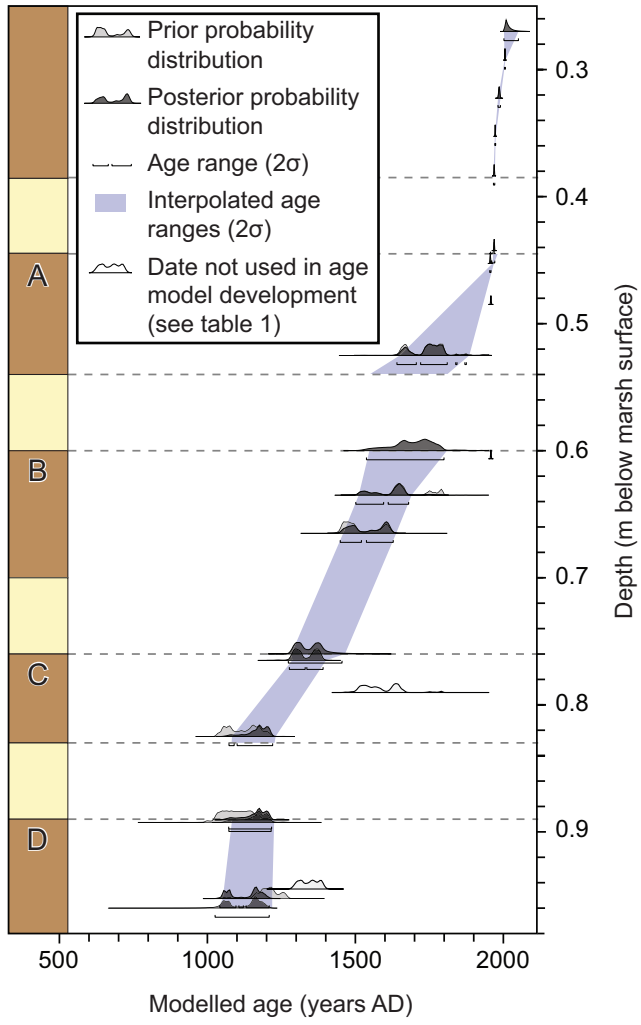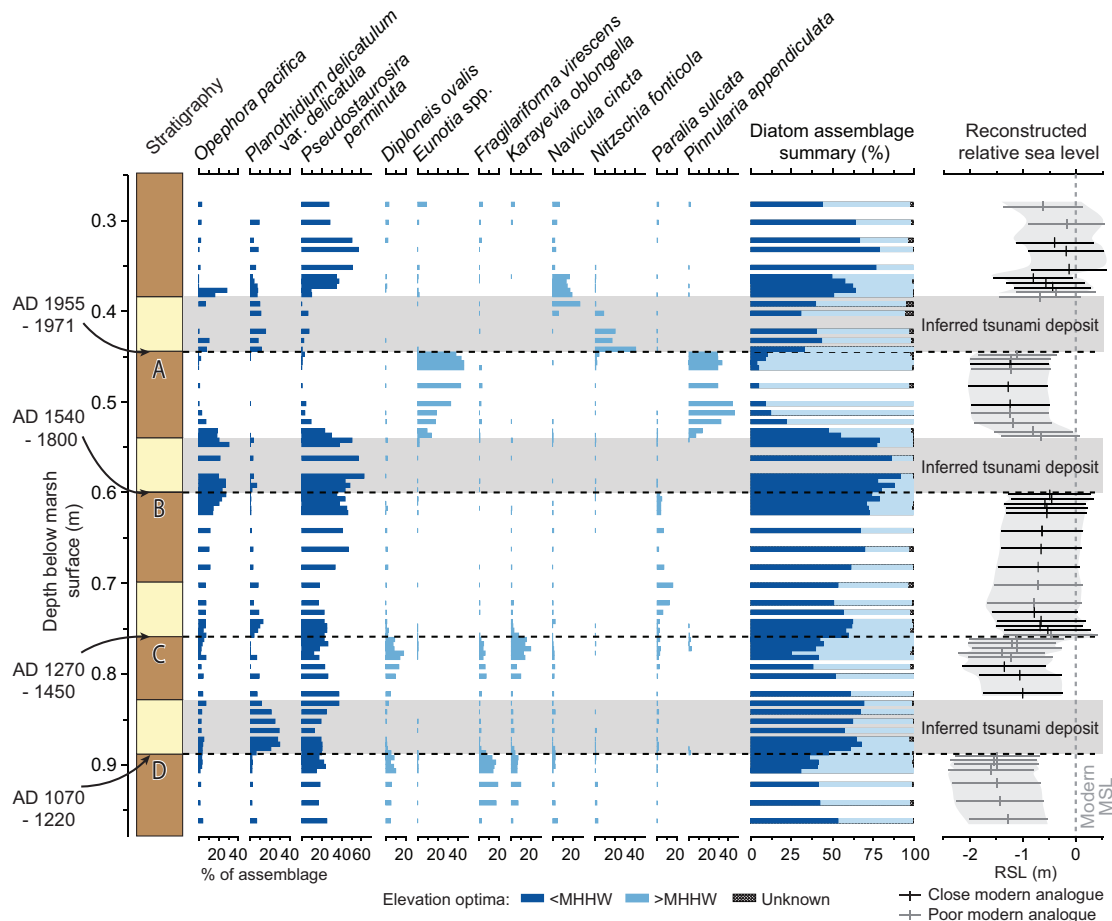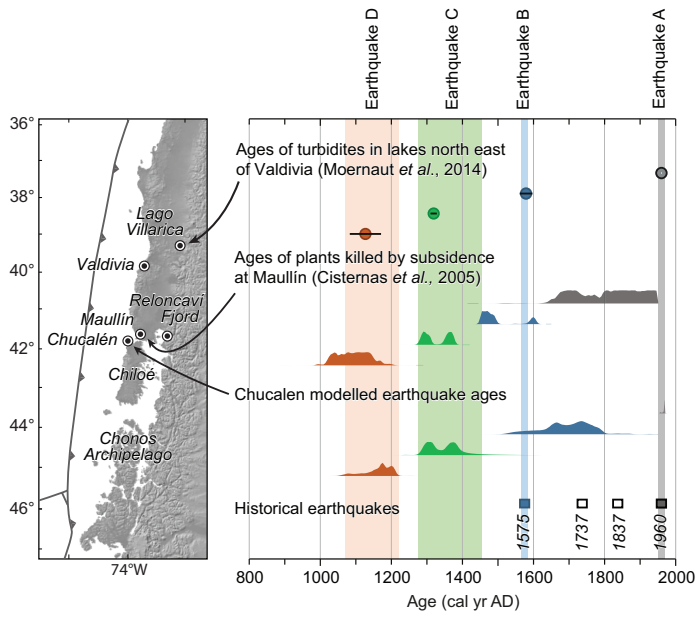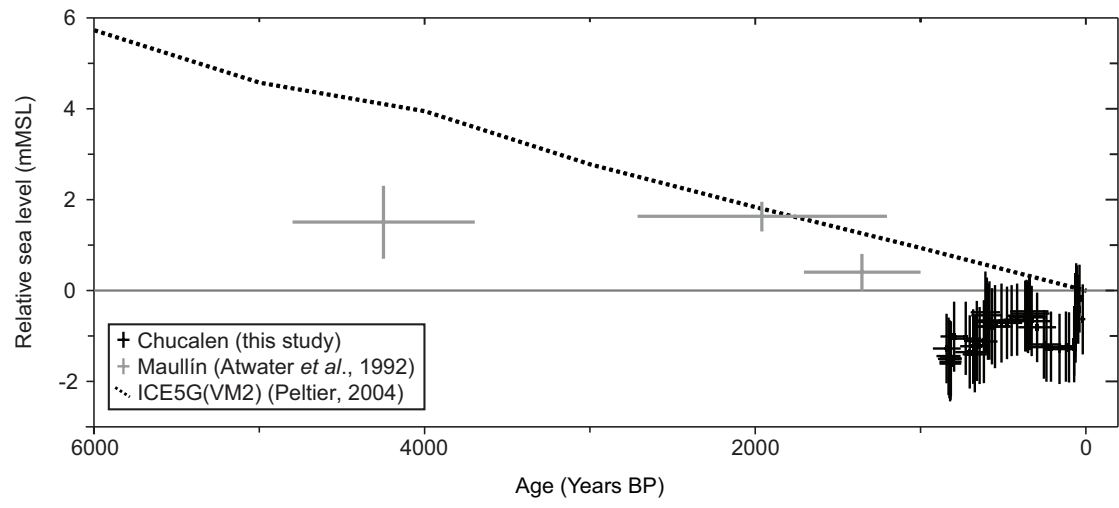
779

Figures

782

783
784

787
788

Earthquake D Earthquake C Earthquake B Earthquake A

Ages of turbidites in lakes north east of Valdivia (Moernaut *et al.*, 2014)

Ages of plants killed by subsidence at Maullín (Cisternas *et al.*, 2005)

Chucalen modelled earthquake ages

Historical earthquakes

1575 1737 1837 1960

Age (cal yr AD)

36°
38°
40°
42°
44°
46°

Lago Villarica
Valdivia
Reloncavi Fjord
Maullín
Chucalén
Chiloé
Chonos Archipelago

74°W

789
790

791
792

Tables

Laboratory code	Sample number	Central depth (cm)	Radiocarbon age (years BP ± 1σ/ F^{14}C ± 1σ)	Calibrated age range (2σ years AD)	*P_sequence* modelled age (2σ years AD)	Posterior probability of being an outlier	Agreement index
Chucalén radiocarbon samples							A$_{overall}$ = 69.1
SUERC-39263	CH11/R1	29.25	1.0646 ± 0.0065	2004-2006 [a]	2004-2006	0.01	86.7
SUERC-39264	CH11/R2	32.25	1.2056 ± 0.0076	1982-1990 [a]	1982-1990	0.01	100.5
SUERC-39265	CH11/R3	35.25	1.4537 ± 0.0092	1971-1973 [a]	1971-1974	0.04	86.8
SUERC-39266	CH11/R4	38.25	1.5337 ± 0.0097	1967-1971 [a]	1966-1971	0.01	100.7
SUERC-39269	CH11/R5	45.25	1.0159 ± 0.0064	1954-1958 [a]	1954-1958	0.14	99.7
SUERC-41189	CH11/R6	49.25	1.0964 ± 0.0048	1956-1960 [a]	-	0.20	-
SUERC-41190	CH11/R7	52.5	234 ± 35	1636-1950 [b]	1641-1875	0.21	104
SUERC-43050	CH11/R8	60.5	1.1042 ± 0.0052	1956-1960 [a]	-	0.85	-
SUERC-43051	CH11/R9	63.5	285 ± 38	1505-1800 [b]	1501-1680	0.04	112.6
SUERC-43052	CH11/R10	66.5	427 ± 38	1441-1626 [b]	1449-1628	0.04	90.9
SUERC-41191	CH11/R11	76.5	713 ± 35	1278-1391 [b]	1277-1391	0.07	98.9
SUERC-43048	CH11/R12	79.5	317± 38	1487-1794 [b]	-	0.98	-
SUERC-41187	CH11/R13	82.5	950 ± 35	1037-1209 [b]	1072-1221	0.34	89.6
SUERC-39270	CH11/R14	89.25	979 ± 51	1020-1210 [b]	1072-1216	0.15	76.7
SUERC-40031	CH11/R15	92.25	680 ± 37	1290-1396 [b]	-	0.90	-
SUERC-40032	CH11/R16	95.25	881 ± 37	1070-1275 [b]	1042-1210	0.09	50.6

794 [a] Calibrated using the post-bomb atmospheric southern hemisphere ^{14}C curve (Hua and Barbetti,

795 2004)

796 [b] Calibrated using SHCal13 (Hogg *et al.*, 2013)

797

798 Table 1: Calibrated radiocarbon dates from plant macrofossils from the Chucalén exposure.

799 Dates modelled in a *P_sequence* deposition model in OxCal 4.2 (Bronk Ramsey, 2009), with a

800 k value of 50. Outlier analysis provides the posterior probability of each sample being an

801 outlier; prior probabilities set to 0.05; posterior probabilities exceeding 0.4 considered to be

802 significant outliers. The age of samples CH11/R6, CH11/R8, CH11/R12 and CH11/R15 do not

803 fit in with the stratigraphic sequence and are not used in age model development.

Earthquake associated with burial of Soil	Magnitude of coseismic deformation (m ± 2σ)
A	-1.12 ± 1.04
B	0.08 ± 1.07
C	-0.92 ± 1.20
D	-0.60 ± 1.10

804

805   Table 2: Vertical coseismic deformation estimates for the four earthquakes obtained by

806   calibrating Chucalén diatom assemblages with the south central Chile transfer function

807   model (Garrett *et al*., 2013). Uplift is positive, subsidence is negative. Estimates are

808   corrected for sedimentation.

Supplementary Info

810
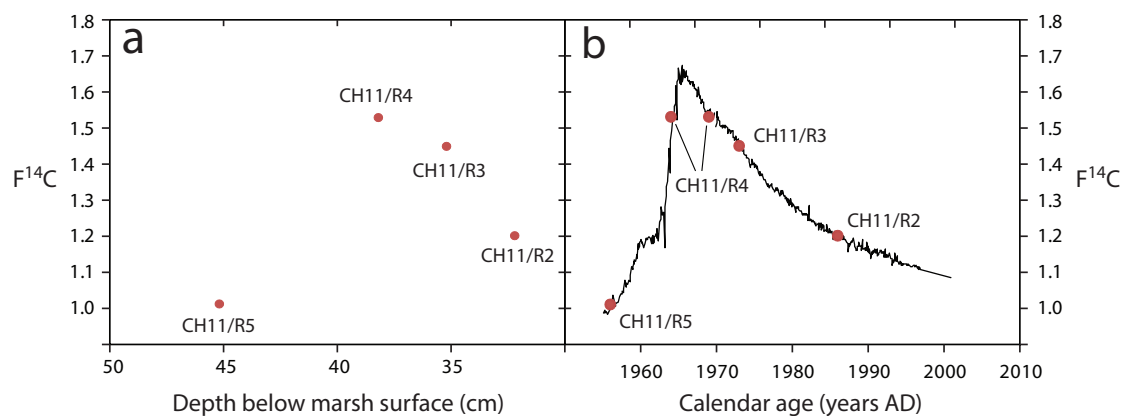
Figure S1: Chucalén bomb spike samples, a. plotted as F14C against depth below the marsh

surface and b. fitted to the post-bomb atmospheric southern hemisphere 14C curve (black

line) of Hua and Barbetti (2004). Sample CH11/R5 must lie on the rising limb, sample

CH11/R4 may lie on either the rising or the falling limb and samples CH11/R3 and CH11/R2

must lie on the falling limb.

816
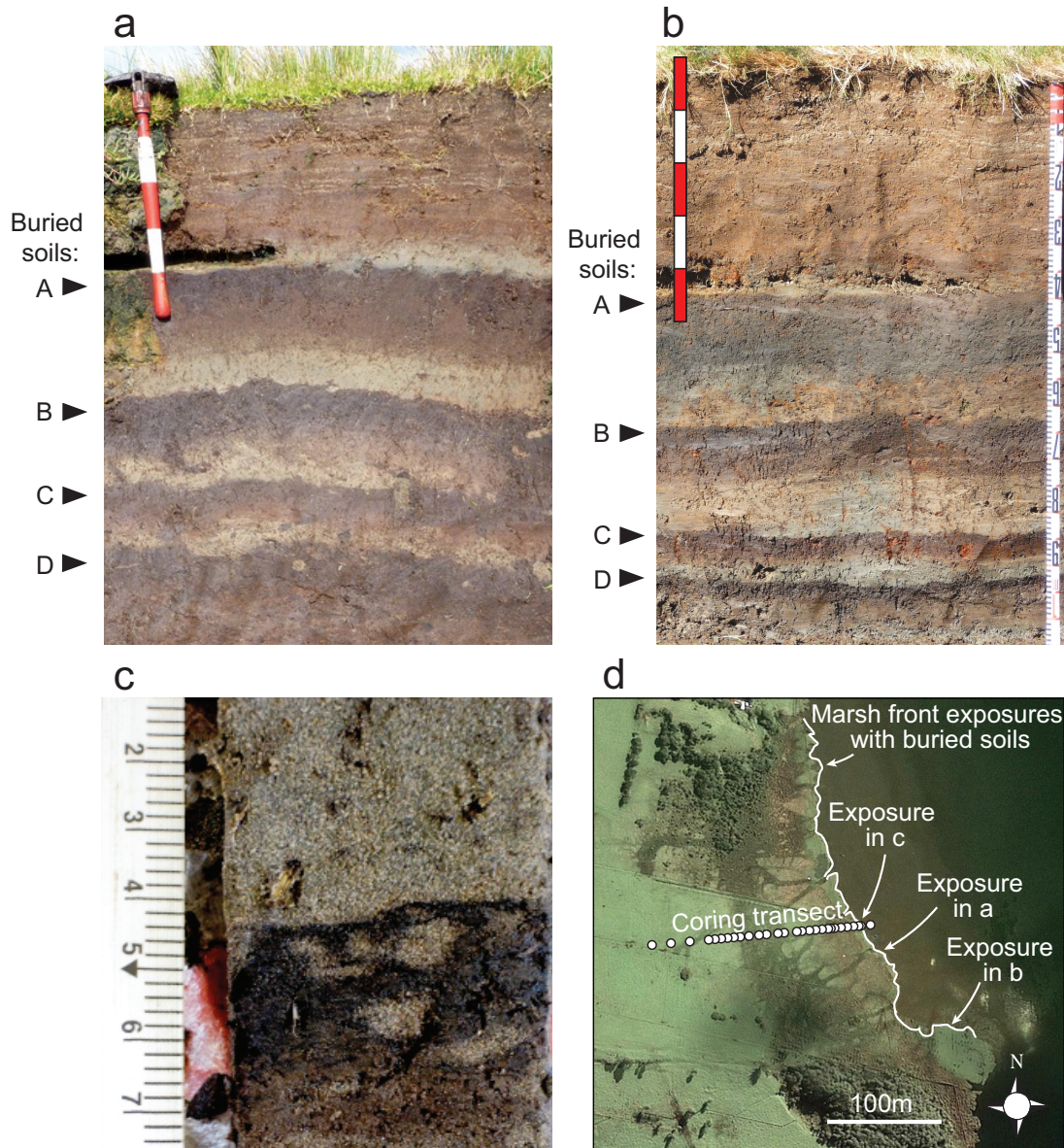
Figure S2: Photographs of Chucalén marsh front exposures. a. and b. display the four buried soils, labelled A-D, in exposures south east of the coring transect. Divisions on scale bars = 10 cm. c. The upper contact of Soil C, displaying burrows filled with the overlying silty sand. d. Map showing the extent of marsh front exposures with visible buried soils, the locations of photographed exposures and the coring transect illustrated in Figure 3.